RESEARCH ARTICLE

ADVANCED FUNCTIONAL MATERIALS
www.afm-journal.de

Check for updates

16163028, 2021, 46, Downloaded from https://onlinelibrary.wiley.com/doi/10.1002/adfm.202103936 by CochraneItalia, Wiley Online Library on [29/12/2022]. See the Terms and Conditions (https://onlinelibrary.wiley.com/terms-and-conditions) on Wiley Online Library for rules of use; OA articles are governed by the applicable Creative Commons License

Hybrid Devices by Selective and Conformal Deposition of $PtSe_2$ at Low Temperatures

*Maximilian Prechtl, Shayan Parhizkar, Oliver Hartwig, Kangho Lee, Josef Biba, Tanja Stimpel-Lindner, Farzan Gity, Andreas Schels, Jens Bolten, Stephan Suckow, Anna Lena Giesecke, Max C. Lemme, and Georg S. Duesberg**

2D materials display very promising intrinsic material properties, with multiple applications in electronics, photonics, and sensing. In particular layered platinum diselenide has shown high potential due to its layer-dependent tunable bandgap, low-temperature growth, and high environmental stability. Here, the conformal and area selective (AS) low-temperature growth of layered $PtSe_2$ is presented defining a new paradigm for 2D material integration. The thermally-assisted conversion of platinum which is deposited by AS atomic layer deposition to $PtSe_2$ is demonstrated on various substrates with a distinct 3D topography. Further the viability of the approach is presented by successful on-chip integration of hybrid semiconductor devices, namely by the manufacture of a highly sensitive ammonia sensors channel with 3D topography and fully integrated infrared-photodetectors on silicon photonics waveguides. The presented methodologies of conformal and AS growth therefore lay the foundation for new design routes for the synthesis of more complex hybrid structures with 2D materials.

M. Prechtl, O. Hartwig, K. Lee, J. Biba, T. Stimpel-Lindner, A. Schels, G. S. Duesberg
Institute of Physics
Faculty of Electrical Engineering and Information Technology
Universität der Bundeswehr München
85577 Neubiberg, Germany
E-mail: duesberg@unibw.de

S. Parhizkar, S. Suckow, A. L. Giesecke, M. C. Lemme
AMO GmbH
Advanced Microelectronics Center Aachen (AMICA)
Otto-Blumenthal-Str. 25, 52074 Aachen, Germany

S. Parhizkar, J. Bolten, M. C. Lemme
Chair of Electronic Devices
RWTH Aachen University
Otto-Blumenthal-Str. 2, 52074 Aachen, Germany

F. Gity
Tyndall National Institute
University College Cork
MicroNano Systems Centre
Lee Maltings, Dyke Parade, Cork T12 R5CP, Ireland

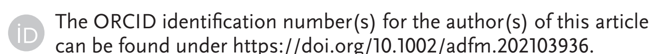
The ORCID identification number(s) for the author(s) of this article can be found under https://doi.org/10.1002/adfm.202103936.

© 2021 The Authors. Advanced Functional Materials published by Wiley-VCH GmbH. This is an open access article under the terms of the Creative Commons Attribution-NonCommercial-NoDerivs License, which permits use and distribution in any medium, provided the original work is properly cited, the use is non-commercial and no modifications or adaptations are made.

DOI: 10.1002/adfm.202103936

1. Introduction

2D materials are at the forefront of material research. Besides graphene[1] and black phosphorus[2] in particular compound 2D materials such as transition metal dichalcogenides (TMDs) have been proposed for many future electronic,[3] photonic,[4,5] optoelectronic devices[6,7] or sensor devices.[8] High-performance devices based on TMDs have been demonstrated in virtually every field of nanotechnology, such as field-effect transistors (FETs),[9] ultraviolet (UV) to infrared (IR) photodetectors,[10,11] micro- and nanoelectromechanical systems (MEMS/NEMS),[12,13] and gas sensors.[14,15] Moreover, newly discovered 2D materials and their heterostructures continue to reveal unique physical phenomena and well observable quantum effects.[16]

A major bottleneck towards real-life applications of 2D materials is the lack of a viable integration technology with high process control and large yield.[17] Even though there have been large progress in the controlled synthesis of 2D materials on specific growth substrates and their subsequent transfer, numerous challenges remain towards more complex devices and systems. Here, we propose several integration routes for 2D materials with distinct advantages over the current state of the art.

Conformal deposition is widely used in semiconductor manufacturing, but not attainable with the common growth-and-transfer approach for 2D materials. It allows the coating of 3D, topological surfaces and thus enables fabricating sophisticated devices that exceed the planar limits, such as FinFETs, MEMS/NEMS, or memory cells.[18] Even though the state of the art for 2D film transfer has somewhat matured,[17] the approach is obviously barely suitable for coating topological surfaces as they have to be mirrored and aligned with the transfer stamps, to avoid bridging and tearing of the transferred films. Here, we demonstrate instead the growth of 2D films directly on the target substrates, including conformal coating.

Another common technique in advanced semiconductor manufacturing is area selective (AS) growth, which enables bottom-up processes for building complex structures and devices.[19–22] Atomic layer deposition (ALD) processes are particularly suited for AS growth because their controlled surface chemistry can be exploited to achieve not only conformality

on 3D structures but also selectivity regarding the growth surface material.[21–23] With this self-aligned method, in which the film only forms on pre-defined areas, vertical structures can be built without additional processing steps such as lithography, etching, or transfer. This is not feasible with the conventional transfer approaches for atomically thin 2D materials,[24] but demonstrated here.

The third prerequisite for 2D material integration is a low thermal budget for synthesis and processing. Recently, the low-temperature formation of the 2D noble metal dichalcogenide platinum diselenide was reported.[25,26] It has been derived from sputtered or evaporated thin Pt layers at temperatures below 450 °C allowing even direct growth on plastics.[13] This low-temperature budget is regarded as a crucial threshold for the use of new materials in electronics, as it allows for back-end-of-line (BEOL) integration in state-of-the-art silicon production lines.[27,28] The remarkable properties of $PtSe_2$, leading to numerous potential applications have been recently reviewed.[29] In short, $PtSe_2$ which undergoes a semimetal to semiconductor transition when thinned to a few layers,[30,31] has shown to have high potential in transistors,[32] chemical sensing,[25] IR-photodetection,[33,34] and piezoresistive sensors.[12] However, sputtering and evaporation processes offer a lower degree of conformality compared to ALD, leaving the highly demanded 3D unattainable. Moreover, $PtSe_2$ has shown to be highly stable in air which is a prerequisite for most applications.[35,36]

Here, we demonstrate the conformal and AS deposition of layered $PtSe_2$ by low temperature thermal assisted conversion (TAC) of ALD deposited Pt. This enables a 2D material that is directly grown on the target substrate, independent of the topography, using the conformality of ALD to overcome the limitation to lateral device structures.[37] Furthermore, AS-ALD of $PtSe_2$ enables the bottom-up, templated definition of device structures already in the growth step. We demonstrate the viability of our methodology with IR photodetectors directly integrated in 3D silicon photonic waveguides and a highly sensitive chemical sensor that utilizes enhanced surface areas through deep trenches covered in $PtSe_2$.

2. Results and Discussion

2.1. $PtSe_2$ Growth by ALD and TAC

TAC of thin metal layers is a universal growth approach that has shown great success in yielding large-scale and continuous layered 2D films with controlled thicknesses at low thermal budgets.[25,38,39] TAC growth in general consists of two steps, the first one being deposition of a metal layer, for instance by physical vapor deposition like sputtering or evaporation. This is followed by its conversion at elevated temperatures with vaporized elemental chalcogenides or chalcogenide compounds. The resulting layered films (Figure S1, Supporting Information) are polycrystalline with nanometer-scale domain sizes.[13,25]

To overcome the physical limitations of the aforementioned metal deposition techniques we employ ALD of Pt, allowing us to grow conformally on 3D substrates. Our process flow is illustrated in **Figure 1**a. The target substrate (Step 1) is coated by Al_2O_3 using ALD (Step 2). The Pt layer is deposited using ALD by alternating pulses of Trimethyl(methylcyclopentadienyl)-platinum(IV) and oxygen (Step 3). TAC at 450 °C is then used to convert the deposited metal layers to $PtSe_2$ (Step 4) using Se as a solid-state precursor (see also methods section).

The thickness of the Pt layer, and, therefore, the thickness of the resulting $PtSe_2$ layer, is controlled by the number of ALD cycles (Figure S1, Supporting Information). Even though platinum ALD is known to suffer from Ostwald ripening,[40,41] TAC leads to a full reformation of the film, resulting in a polycrystalline and continuous $PtSe_2$ layer (Figure S2, Supporting Information).

Raman spectroscopy has been carried out on flat substrates to confirm the formation of $PtSe_2$ from the ALD grown Pt. Raman spectra of four different $PtSe_2$ film thicknesses are presented in Figure 1b. All spectra show two modes at wavenumbers of 175 and 210 cm^{-1} associated with the E_g and A_{1g} modes of $PtSe_2$, respectively. For increasing film thicknesses, we observe a redshift of the modes (indicated as dashed orange lines) and an increase of the E_g/A_{1g} intensity ratio. These changes have been reported before and are typical for thin films of $PtSe_2$.[42]

In Figure 1c and Figure 1d, the X-ray photoelectron spectroscopy (XPS) spectra of the selenium 3d and platinum 4f core level region of flat samples are depicted. The Pt4f region consists of three sets of doublets, with the main contribution indicating that 80 % of the Pt atoms are present in the form $PtSe_2$. The remaining two doublets contributing with 4 % and 16 % can be attributed to a substoichiometric form ($PtSe_x$) and oxidation (PtO_x), respectively. It is worth noting that the two doublets are only present at the surface layer of platinum atoms, where a loss of selenium atoms due to degradation ($PtSe_x$), and, therefore, oxidation (PtO_x) is expected.[43] The Se3d region consists of three doublets and one singlet. Similar to the Pt4f, the main contribution corresponds to 72 % of the Se atoms bound to Pt atoms in the form of $PtSe_2$ while 17 % of the Se atoms are present in substoichiometric $PtSe_x$.[44] The third doublet indicates that 11 % of the Se atoms are oxygen bound (SeO_x). Finally, the singlet corresponds to the Pt 5p orbital. The overall stoichiometric ratio of Pt to Se is 1:2, supporting the Raman data which have shown growth of high-quality $PtSe_2$. We furthermore acquired and analyzed a survey spectrum, which did not show any significant other components (Figure S3, Supporting Information). To investigate the alignment of our grown film, we acquired high-resolution cross-sectional transmission electron microscopy (HR X-TEM) images (Figure 1e). The layered structure of the material is clearly visible, moreover, the layers are well aligned with the substrate surface. We therefore can conclude, taking into account Raman, XPS, and HR-X-TEM analysis, that combination of Pt-ALD and TAC yields high-quality and layered $PtSe_2$ films.

2.2. Conformal Deposition of $PtSe_2$ on Topological Substrates

The conformality of the ALD-based $PtSe_2$ growth has been investigated on substrates with a distinct topography. We prepared substrates by cutting 66 trenches into flat silicon wafers with a width of 40 µm and a depth of 140 µm resembling an aspect ratio of 3.5 (**Figure 2**a,b). After ALD deposition of 20 nm Al_2O_3, platinum has been deposited and selenized as described above. We chose a relatively thick $PtSe_2$-layer (200 cycles with higher Pt-precursor pressure) to enhance

© 2021 The Authors. Advanced Functional Materials published by Wiley-VCH GmbH

16163028, 2021, 46, Downloaded from https://onlinelibrary.wiley.com/doi/10.1002/adfm.202103936 by CochraneItalia, Wiley Online Library on [29/12/2022]. See the Terms and Conditions (https://onlinelibrary.wiley.com/terms-and-conditions) on Wiley Online Library for rules of use; OA articles are governed by the applicable Creative Commons License

16163028, 2021, 46, Downloaded from https://onlinelibrary.wiley.com/doi/10.1002/adfm.202103936 by CochraneItalia, Wiley Online Library on [29/12/2022]. See the Terms and Conditions (https://onlinelibrary.wiley.com/terms-and-conditions) on Wiley Online Library for rules of use; OA articles are governed by the applicable Creative Commons License

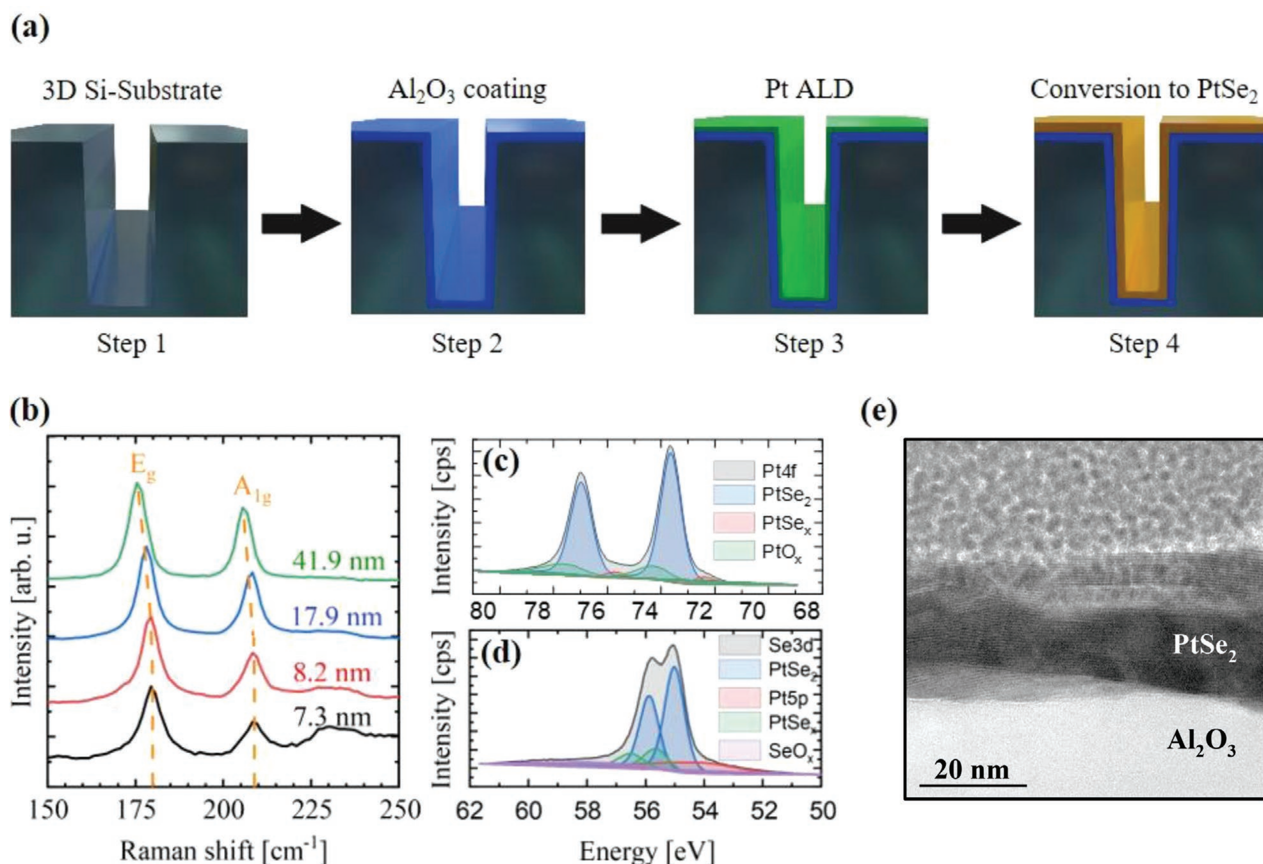

Figure 1. Low-temperature $PtSe_2$ growth on structured substrates. a) Process flow: After deposition of Al_2O_3 by ALD on the target substrate (Step 2), the (structured) substrate is decorated with Pt using ALD (Step 3). In the last step, the sample is converted to $PtSe_2$ using TAC (Step 4). b) Raman spectra of $PtSe_2$ for four different thicknesses. Spectra have been normalized to the $PtSe_2$ E_g mode. c) XPS spectrum for Pt4f and d) Se3d region of a 70 nm thick $PtSe_2$ film. e) HR X-TEM image of an as-grown $PtSe_2$ film. The layered structure is clearly visible.

visibility in cross-sectional scanning electron microscopy (X-SEM) and X-TEM. Figure 2c shows an X-SEM image of one coated trench. We compared X-SEM and X-TEM images acquired from the top (Figure 2d,g), the side (Figure 2e,h), and the bottom (Figure 2f,i) regions of the trench-structured samples. For all investigated areas, two different $PtSe_2$ species can be identified. The first regime of grown material shows a horizontal alignment with the target substrate, while the remaining $PtSe_2$ grows in a vertical direction on top of the layered material. The transition of the growth regimes is marked with a white dashed line in Figure 2g–i. This phenomenon of changing growth alignment for different thicknesses in TAC-grown TMD films has been reported previously.[45,46] It can be explained with a change in surface energy: Vertical growth is preferred when the surface energy of the grown material becomes more dominant with increasing initial metal layer thickness.[46] For the top, side, and bottom areas, we identified an average thickness of 20 nm for the $PtSe_2$ grown in the first regime. This layer of well-aligned $PtSe_2$ is covered by unaligned $PtSe_2$, grown predominantly vertical with respect to the initial surface and with a thickness of up to 50 nm in the top region and less for the bottom area of the trench. Independent of these vertically aligned layers, which are thinner in the bottom of the trench than on the top, we conclude that layered 2D and well-aligned $PtSe_2$ has been grown conformally in all three regions despite the challenging substrate topology.

2.3. Ammonia Gas Sensing with Topological Sensors

2D materials have been proposed for chemical sensing due to their large surface-area-to-volume ratio. Numerous reports on chemi-resistors or chemical field-effect transistors (ChemFETs) with graphene,[47] BP,[48] and TMDs[49] demonstrating high sensitivities have been published. In particular, $PtSe_2$ has shown great potential in chemical sensing for NO_2 as reported[25] and also theoretically predicted.[50] Herein we established the sensitivity of our $PtSe_2$ TAC-grown films towards NH_3, a gas that is known to be more difficult to detect with TMD films compared to NO_2. As only the surface of the material of choice can be used as an active sensing area, one can reduce the physical sample size using 3D topographic samples, and therefore enable packaging of more active material within less lateral physical space. Starting from the 3D trenched samples shown in Figure 2a, we realized electrical contacts by sputter deposition of 30 nm Pt using a shadow mask, forming an effectively 2.8 cm long channel while only taking 1.1 cm of lateral length.

© 2021 The Authors. Advanced Functional Materials published by Wiley-VCH GmbH

16163028, 2021, 46, Downloaded from https://onlinelibrary.wiley.com/doi/10.1002/adfm.202103936 by CochraneItalia, Wiley Online Library on [29/12/2022]. See the Terms and Conditions (https://onlinelibrary.wiley.com/terms-and-conditions) on Wiley Online Library for rules of use; OA articles are governed by the applicable Creative Commons License

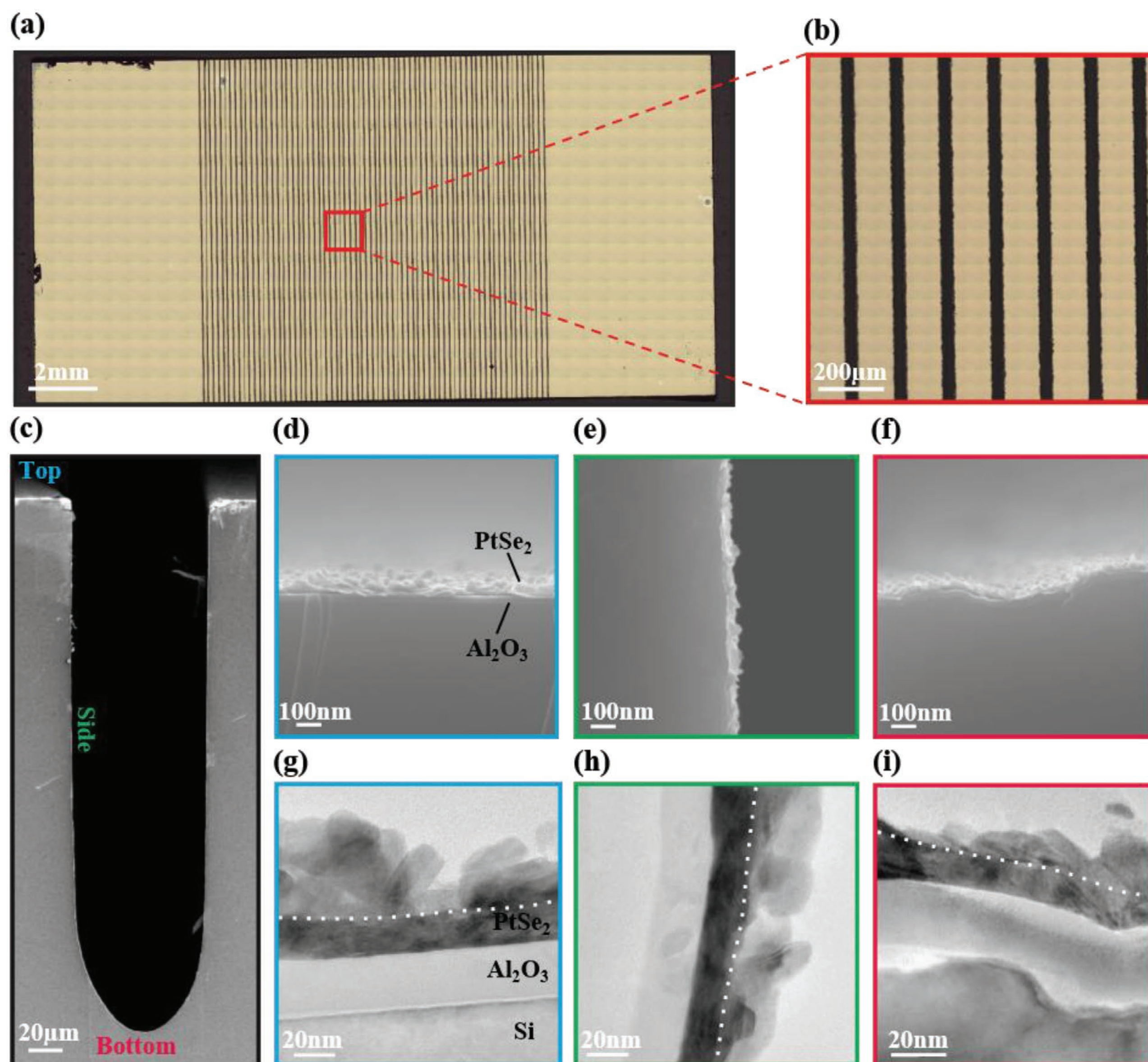

Figure 2. Conformal deposition of $PtSe_2$ in trenches. a) Top view optical microscopy image of the 2×1 cm^2 Si chip, with 66 trenches fabricated using a mechanical dicing saw b) Magnified optical image of the region highlighted in (a) showing individual trenches. c) SEM image of the cross-section of a trench with an aspect ratio of 3.5. d–f) X-sectional SEM images of top (blue frame), side (green frame) and bottom (red frame) of a trench after deposition of Al_2O_3 and $PtSe_2$ (bright contrast) (c). g–i) X-sectional TEM images at top (blue frame), side (green frame), and bottom (red frame) of a trench after deposition of Al_2O_3 and $PtSe_2$. The layered and approximately 20 nm thick $PtSe_2$ region (dark) above the approximately 25 nm layer of Al_2O_3 is highlighted by white dotted line. Above vertically grown $PtSe_2$ with lighter contrast is visible.

For the 80 nm thick $PtSe_2$ film, a resistivity of $\rho = 1.3\times10^{-3}$ Ωcm was derived (Figure S4, Supporting Information).

The performance of the gas sensors based on the conformally grown $PtSe_2$ films was evaluated by measuring the relative resistance changes upon periodic NH_3 gas exposure. The test chamber introduces 100 sccm of NH_3 gas diluted with dry N_2 gas.[39,51,52] **Figure 3**a shows a typical gas sensor response at various concentrations from 0.5 to 8 ppm, where the resistance of the trench-structured $PtSe_2$ increases upon exposure to NH_3. While most resistive gas sensors based on low-dimensional materials commonly suffer from slow recovery kinetics, $PtSe_2$ films show acceptable recovery speed upon NH_3 exposure for 1 min. Gas introduction at a higher concentration requires a much longer recovery time which is noticeable through the not-fully-recovered resistance of $PtSe_2$ sensors after a NH_3 introduction at 8 ppm—unlike the other lower concentrations—in a periodic exposure (1 min for exposure and 5 mins for recovery) of this work. As a result, a baseline drift of sensor response curves was found and we believe that the acceleration of the recovery speed, such as UV illumination[53,54] and higher working temperature,[55] is helpful to attenuate this drifting phenomenon. The limit of detection (LOD) was extracted by simple signal processing based on the signal-to-noise ratio (SNR), as the signal must be at least three times or larger than

© 2021 The Authors. Advanced Functional Materials published by Wiley-VCH GmbH

16163028, 2021, 46, Downloaded from https://onlinelibrary.wiley.com/doi/10.1002/adfm.202103936 by CochraneItalia, Wiley Online Library on [29/12/2022]. See the Terms and Conditions (https://onlinelibrary.wiley.com/terms-and-conditions) on Wiley Online Library for rules of use; OA articles are governed by the applicable Creative Commons License

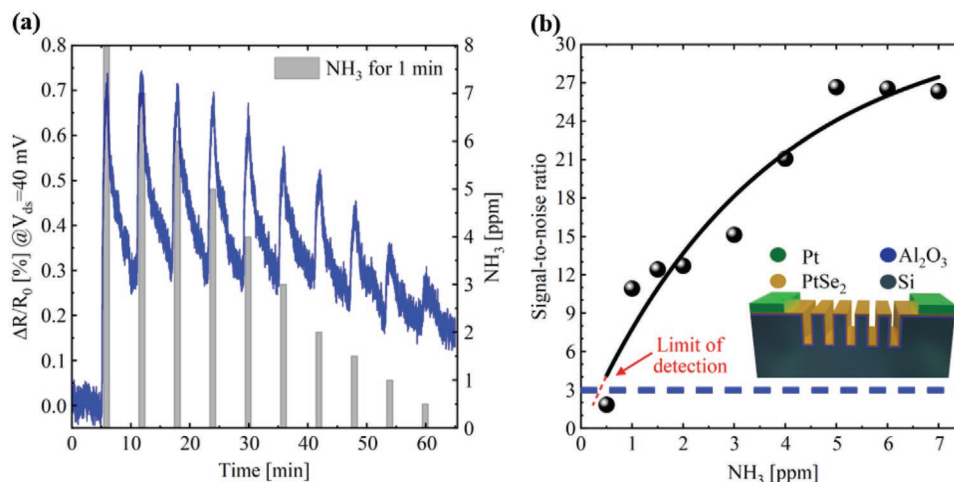

Figure 3. Structured $PtSe_2$ for NH_3 sensing. a) Fast sensor response at room temperature upon periodic declining NH_3 concentrations. b) SNR of sensor at various NH_3 concentrations (dots). The fitted curve (black line) reveals a LOD of 370 ppb for NH_3. Inset: Schematic of the cross-section of the $PtSe_2$ gas sensor.

the root-mean-square noise of the measured device.[56] SNRs at various gas concentrations tend to follow an exponential decay equation based on the isotherm model as shown in Figure 3b. The theoretical LOD can be derived by extrapolation of the fitted curve, through which 370 ppb of NH_3 gas is expected to be detected and experimentally confirmed (Figure S5, Supporting Information). Up to date, only once empirical NH_3 sensitivity of $PtSe_2$ has been briefly mentioned even though it wasn't fully investigated as an NH_3 gas sensor.[57] Our work therefore is the first $PtSe_2$ study that presents an NH_3 LOD for $PtSe_2$.

In previous theoretical and experimental reports of low dimensional material-based gas sensors, NH_3 sensitivity is typically inferior compared to other toxic gases like NO and NO_2, because the sensing mechanism of resistive gas sensors is based on the charge transfer model from analytes in general.[50,55,58–61] Therefore, NH_3 detection is challenging, especially for short exposure time and without activating the reaction through UV illumination or accelerating the recovery time through elevated working temperatures. However, our conformally deposited $PtSe_2$ films show very promising gas sensor performance with much shorter exposure times, even at room temperature, resulting in superior gas sensing abilities.

2.4. Selective Area Deposition of $PtSe_2$ on Aluminum Oxide

The assembly of structures with higher complexity, such as heterostructures and the integration of 2D materials in future devices require patterning and alignment onto target areas. Transfer processes have limited accuracy and conventional top-down approaches like wet- or reactive ion etching require post-growth fabrication steps including resist application, developing, and resist removal. In addition, the remaining residues on top of the grown materials may induce defects and harm the layer quality, and consequently the overall device performance, in particular in ultra-thin 2D materials.[17] Hence, it is favorable to grow the 2D material only in the areas of interest, making a post-growth patterning step redundant.[21,22] AS-ALD of platinum is a pathway to selectively grow metal films only on predefined parts of the substrate and, thus, enabling selective growth of $PtSe_2$ by the subsequent conversion of those layers. One way to gain selectivity during ALD growth is selective precursor adsorption which can be enabled by controlling the chemical surface termination of the growth substrate.[19]

The process flow for AS deposition of $PtSe_2$ is presented in **Figure** 4a. We chose the example of silicon waveguides fabricated from silicon on insulator (SOI) material, which have a certain topography and where both conformality and selective growth can be tested. First, the chips and the waveguides were covered by ALD with 10 nm Al_2O_3. Then, a lithographic step with resist was used to define the regions of interest (Step 1). The Al_2O_3 was wet etched with buffered hydrofluoric acid (BHF), leaving pads of Al_2O_3 on the surface in the areas of the waveguides after resist removal (Step 2). Processing in this way results in a significant difference in the surface chemistry between the Si and Al_2O_3 surface, as the BHF etched Si areas are hydrogen-terminated, that is, hydrophobic,[62] while the Al_2O_3 pads are hydrophilic. Thus, Pt-ALD is selectively seeded on the Al_2O_3 surface (Step 3). The Pt on the Al_2O_3 region is then converted to $PtSe_2$ exactly on the Al_2O_3 region through the TAC process (Step 4). Figure 4b shows a micrograph of a $PtSe_2$ area with a size of 50 × 25 µm² fabricated in this fashion partly covering the silicon waveguide. The presence of $PtSe_2$ was confirmed through chemical XPS mapping. Figure 4c shows the corresponding map of the same area as shown in Figure 4b, revealing a clearly higher response of the Pt4f-peak in the region of the $PtSe_2$ pad than on the silicon. As a measure for the selectivity of our developed process, we calculated the selectivity factor (SF) which is can be defined as

$$\mathrm{SF} = \frac{\theta_{\mathrm{GA}} - \theta_{\mathrm{nGA}}}{\theta_{\mathrm{GA}} + \theta_{\mathrm{nGA}}} \tag{1}$$

Equation (1). Definition of the SF.

where θ_{GA} and θ_{nGA} are the amounts of material presented after deposition on the growth and off the growth areas,

© 2021 The Authors. Advanced Functional Materials published by Wiley-VCH GmbH

16163028, 2021, 46, Downloaded from https://onlinelibrary.wiley.com/doi/10.1002/adfm.202103936 by CochraneItalia, Wiley Online Library on [29/12/2022]. See the Terms and Conditions (https://onlinelibrary.wiley.com/terms-and-conditions) on Wiley Online Library for rules of use; OA articles are governed by the applicable Creative Commons License

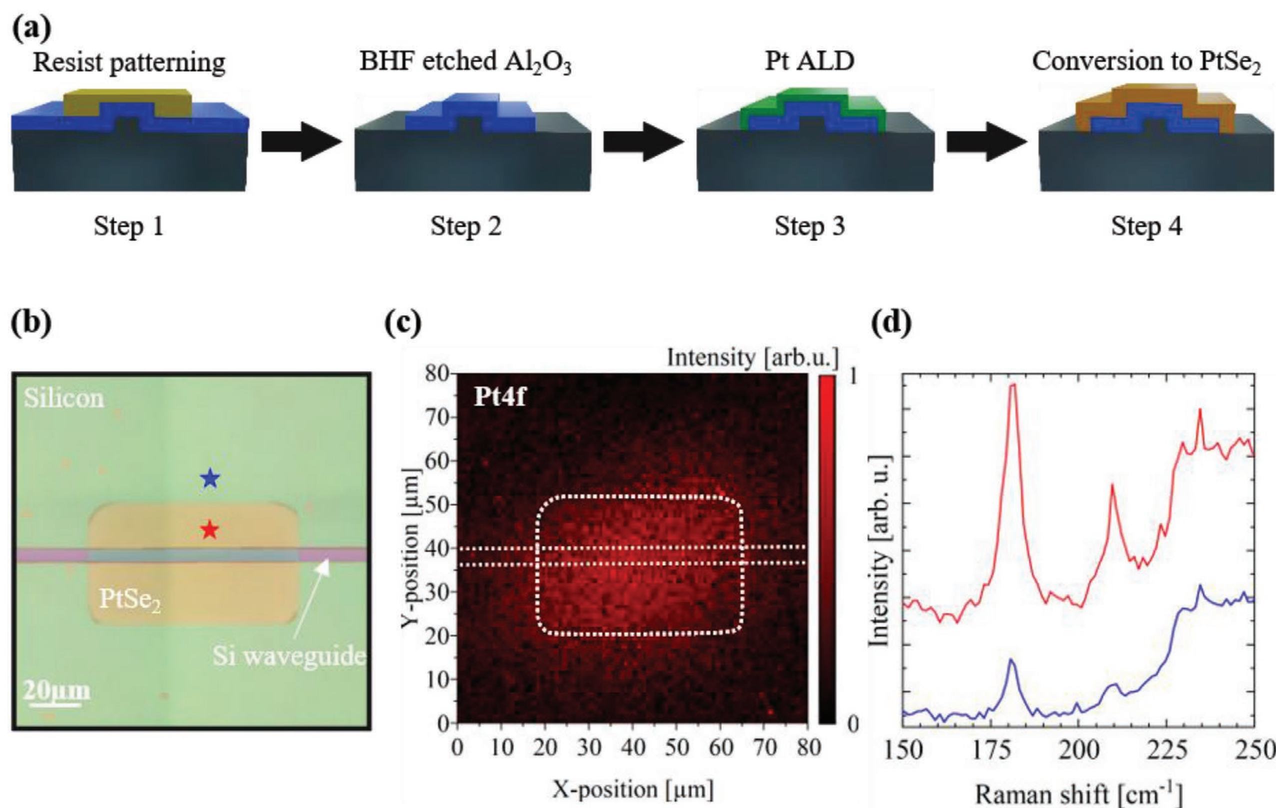

Figure 4. AS deposition of $PtSe_2$. a) Process flow: Step 1: Lithographic patterning of a hard mask on Al_2O_3 covered substrate. Step 2: Wet etch of Al_2O_3 with buffered HF and resist removal. Step 3: AS Pt-ALD on Al_2O_3. Step 4: TAC of Pt with Se to $PtSe_2$. b) Optical microscopy image showing selectively deposited $PtSe_2$ on an Al_2O_3 pad on a silicon waveguide. c) Chemical XPS map of the Pt4f peak of the same region shown in (b) with the $PtSe_2$ area and the Si waveguide highlighted by white dashed lines. d) Raman spectra at points indicated by red and blue stars in (b) showing clearly distinguishable $PtSe_2$ response at the red point only.

respectively.[19,63] Those values can be obtained by extracting the integrated peak area of the Pt4f peak on and off the growth region (Figure 4c) resulting in SF = 0.752 using (Equation (1)). This is further supported by Raman measurements (Figure 4d), which show a much more prominent $PtSe_2$ fingerprint in the channel area compared to the bare Si substrate. Notably, the $PtSe_2$ Raman modes are also present around the deposited $PtSe_2$ pad. This parasitic deposition can be attributed to the exposure of the sample to ambient atmosphere during transportation to the deposition chamber, which partially destroys the hydrogen termination of the silicon by natural oxidation and therefore somewhat lowers the selectivity of the process. Nevertheless, the SF can be significantly improved by dedicated transport systems capable of encapsulating samples under an inert gas atmosphere. Selectivity can also be improved by deposition of thinner $PtSe_2$ films, as in general selectivity gets lowered with an increasing number of deposited (Pt-)ALD cycles.[22]

2.5. On-Chip Integrated IR Photodetector by AS and Conformal Deposition of $PtSe_2$

Thick $PtSe_2$ behaves as a semimetal, but turns into a semiconductor with a bandgap value in near to mid-IR range for mono- to few-layer thickness, making it a promising material for IR photodetection.[32–34] Here, we demonstrate the application of our AS and conformal deposition with IR photodetectors integrated on silicon waveguides. In these structures, light is guided by a rib waveguide with 50 nm step height while in and out-coupling is realized via two grating couplers optimized for 1550 nm wavelength. The $PtSe_2$ patch (Figure 4b), can be used as a photodetector if it is electrically contacted, as shown in the schematic in **Figure 5**a. Here, we used Ni/Al deposited by sputtering and subsequent lift-off, resulting in a 50 μm long and 13 μm wide $PtSe_2$ photodetector channel (Figure 5b). The total detector resistance was 125 MΩ (See Supporting Information for further details).

To measure the photoresponse of the photodetector, laser light at 1550 nm was modulated using an electro-optic modulator at 1 kHz frequency and coupled into the waveguide through a single-mode fiber. The photoresponse of the $PtSe_2$ detector was measured by connecting the output of the contact electrodes to a Lock-In amplifier (Stanford Research Systems SR380), which amplifies the photo-signal (AC signal at 1 kHz) and filters the noise of the system. The bias voltage was applied from the same two contact electrodes to the device. The initial test of functionality was performed by periodically switching the excitation laser on and off. The resulting photovoltage (V_{ph}) response of the as-grown $PtSe_2$ channel is shown in Figure 5c,

 © 2021 The Authors. Advanced Functional Materials published by Wiley-VCH GmbH

16163028, 2021, 46, Downloaded from https://onlinelibrary.wiley.com/doi/10.1002/adfm.202103936 by CochraneItalia, Wiley Online Library on [29/12/2022]. See the Terms and Conditions (https://onlinelibrary.wiley.com/terms-and-conditions) on Wiley Online Library for rules of use; OA articles are governed by the applicable Creative Commons License

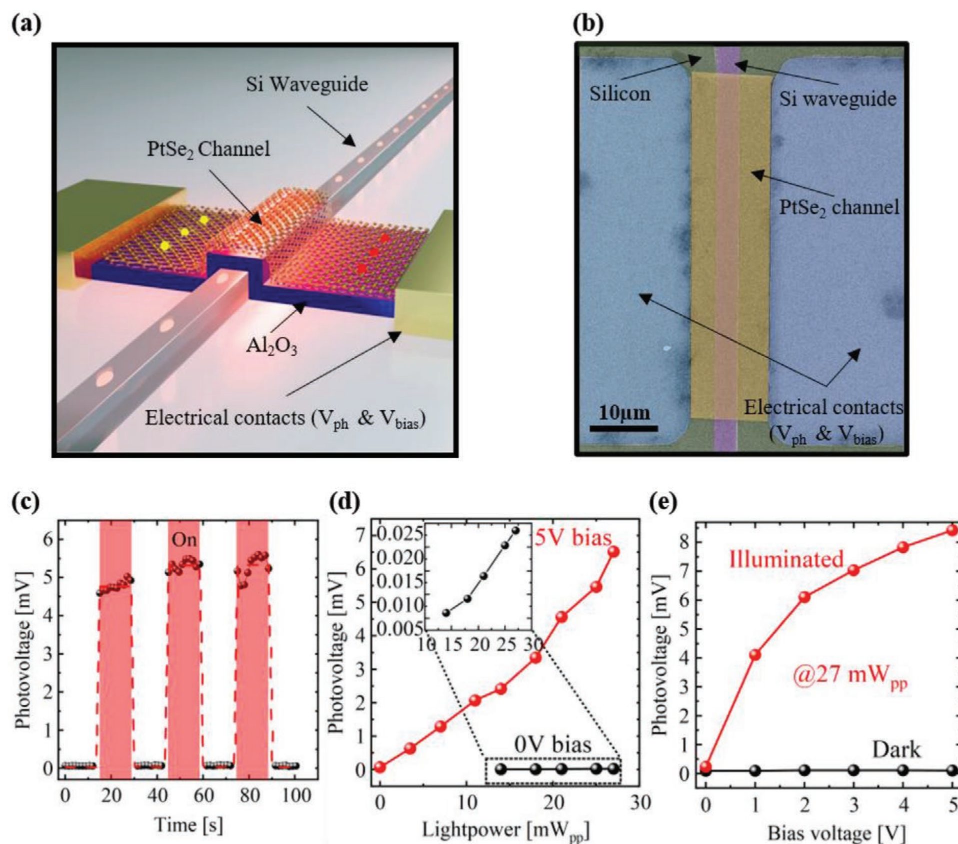

Figure 5. On-chip integrated IR-photodetector created by AS and conformal $PtSe_2$ deposition. a) Schematic of the integrated $PtSe_2$ IR-photodetector on a silicon waveguide. b) Color-enhanced SEM image of the selectively grown and contacted $PtSe_2$ channel. c) Time-resolved photoresponse of the $PtSe_2$ photodetector at 5 V applied bias under pulsed excitation (black) and averaged signal response (red line). On state of the laser is marked as red background. d) Photovoltage versus exciting light power at 0 (black) and 5 V (red) bias voltage. e) Photovoltage versus applied bias voltage at 27 mW_{pp} input laser power for dark (black) and illuminated (red) state.

confirming that the device response is indeed triggered by IR illumination. Furthermore, we find a nearly linear dependence of the extracted photovoltage versus illumination power (Figure 5d). The response is present even without external bias (V_{bias} = 0V), which may be explained with a built-in field due to the work function difference at the $PtSe_2$-Ni/Al interface. The response is enhanced by a factor of ten upon application of V_{bias} = 5 V. Figure 5e shows this in more detail, that is, we plot the dependence of the extracted photovoltage versus the applied bias voltage. In the dark state, we find no significant increase in extracted photovoltage upon increasing V_{bias}, while V_{ph} increases significantly with V_{bias} upon illumination. The responsivity of the $PtSe_2$ photodetector is calculated to be 241 mV W^{-1}, which corresponds to 1.93 nA W^{-1}. This value is limited by the high resistance of the channel. Although the responsivity of this first fully waveguide integrated photodetector is smaller in comparison to graphene photodetectors produced by mechanical exfoliation or epitaxially grown germanium detectors, the advantage of our approach is obvious.[64,65] First, the $PtSe_2$ has been grown directly and selectively on the waveguides without any requirement for planarization of the waveguide. This makes the transfer, post-transfer etching, and patterning processes completely redundant. Second, this has been achieved at BEOL compatible temperatures, which is currently impossible with graphene and with 3D photodetector materials. Third, the conformal growth process enables the coating of arbitrary waveguide (or substrate) shapes without extensive strain, where transfer-based approaches reach clear physical limits. Furthermore, the thickness-dependent bandgap of $PtSe_2$ may be utilized to reduce the photodetector's dark current significantly, promising better SNRs compared to graphene. Finally, AS and conformal ALD of platinum and TAC are easily scalable to arbitrary size.

3. Conclusion

The conformal and AS deposition of large-scale, layered $PtSe_2$ films by combining ALD of platinum with TAC is shown. Raman spectroscopy, XPS, X-SEM, and X-TEM reveal the high quality, conformality, and area selectivity of the deposition. As it is based on ALD it is highly versatile towards other substrates, materials, and topographies. The TAC process can be scaled-up and due to its low-temperature budget, it is fully compatible with BEOL semiconductor fabrication.

The versatility and applicability of our newly developed methodology are demonstrated by the fabrication of an on-chip ammonia gas sensor and a fully waveguide-integrated

 © 2021 The Authors. Advanced Functional Materials published by Wiley-VCH GmbH

$PtSe_2$ IR-photodetector. The 3D structured gas sensor showed an outstanding LOD of 370 ppb for the detection of NH_3. The combination of conformal and AS deposition was exploited to directly grow $PtSe_2$ on pre-defined areas on Si-waveguides as an active channel for IR-photodetection. It performed at $\lambda = 1550$ nm and showed photovoltages up to 241 mV W^{-1}. It may be improved by optimization and completely working in inert atmosphere. The AS and conformal deposition of $PtSe_2$ presented in this work will be applicable to further 2D materials and other topologies to create further complex structures and devices. Thus these processes will allow new design routes for manufacturing of future nanodevices based on 2D materials.

4. Experimental Section

Synthesis of $PtSe_2$ by Pt ALD and TAC: For all deposition processes, a custom-built cold-wall reactor (ATV) was used, fully encapsulated in a glovebox filled with N_2 (<1 ppm H_2O and O_2). On silicon substrates, a dielectric layer of Al_2O_3 was deposited using a standard ALD process by alternating TMAH (25 wt. % in water) and H_2O pulses at 1 mbar process pressure and 200 °C process temperature. Platinum ALD was carried out at a pressure of 0.5 mbar, at a substrate temperature of 250 °C. (Trimethyl)methylcyclopentadienylplatinum(IV) (99%, Strem Chemicals) heated up to a temperature between 50 (all processes except trench-structured samples) and 65 °C (for trench-structured samples) and pure oxygen with a flow of 80 sccm were used as precursor sources with pulse times of 2 and 5 s, respectively. In between the precursor steps the reactor was purged for 30 s using N_2 (purity 6.0) with a flow of 60 sccm. Subsequent TAC was performed at process temperatures of 450 °C substrate temperature and 4 mbar process pressure. Pure selenium powder (>99.5%, VWR) was heated up to 220 °C and transported toward the sample with a flow of 50 sccm hydrogen, taking 120 min in total. All 3 processes, meaning deposition of Al_2O_3 seeding layer, Pt-ALD, and subsequent conversion to $PtSe_2$ were carried out in the same chamber.

Characterization by Raman and X-Ray Photoelectron Spectroscopy: Raman data was collected using a WITec Alpha 300 Confocal Raman system, using 532 nm excitation wavelength and 3 mW laser power on the sample surface with a 100x objective (NA = 0.9) The grating used for Raman measurements had 1800 grooves per mm. XPS data were acquired using a Physical Electronics Versa Probe XPS tool. This system uses the monochromated Al Kα line (1486.7 eV). For single spectra acquisition, a spot size of 100 µm with a beam-power of 96.7 W was used, while for chemical XPS mapping a spot size of 20 µm with a power of 4.6 W was used. The spectra have been fitted using Gaussian–Lorentzian fit functions. For chemical XPS mapping, a spot size of 20 µm with a power of 96.7 W was used.

Cross-Sectional Imaging with Scanning and Transmission Electron Microscopy: For the acquisition of X-SEM images, a JEOL JSM 6700F was used with an acceleration voltage of 10 kV. Cross-sections of the samples were prepared by mechanical cleaving. For cross-sectional transmission electron microscopy (X-TEM) analysis a JEOL JEM-2100 at 200 kV in bright field mode was used. The lamellas have been prepared using a Dual Beam Focused Ion Beam (FIB) FEI Helios NanoLab 600i. A 50 nm carbon layer, followed by a 300 nm platinum layer were deposited within the Dual Beam FIB by electron beam-induced deposition and a 2 µm carbon layer was deposited by ion-beam-induced deposition. Those three layers were deposited for the protection of the samples during milling process. The lamella was prepared and thinned down to less than 200 nm thickness. The thinning at 30 kV was finished by polishing at 5 kV to reduce the ion-beam-induced damage to a region smaller than 2 nm at both sides (final thinning at 93 pA and 30 kV, final polish at 2 kV and 28 pA).

Selective Deposition of $PtSe_2$ and Subsequent Fabrication of $PtSe_2$ Photodetectors: Photonic rib waveguides and grating couplers were fabricated on a commercial silicon-on-insulator substrate (Top Si crystal axis: 100) with 220 nm top silicon using electron beam lithography and reactive ion etching. The waveguide core was 3 µm wide and was formed by a 50 nm step. The waveguide supports multiple modes, but only the fundamental TE mode was excited by the grating coupler and no mode conversion was expected, as the waveguides were completely straight. The grating couplers have typical losses of 3.5 dB before and 4.5 to 6 dB after AS-$PtSe_2$ deposition. An Al_2O_3 coating of 10 nm thickness was deposited using Al_2O_3 ALD process. Resist was applied and structured by optical lithography leaving pads of resist on top of the Al_2O_3 surface after developing. Samples were dipped into BHF solution for 45 s. Removal of the resist was done by N-Methly-2-pyrrolidone (5 min, 55 °C), acetone (5 min, 55 °C), and isopropanol (5 min, 55 °C) after which the samples were transported to the deposition chamber while keeping the exposure to ambient conditions below 5 min. Deposition was performed as described above.

Supporting Information

Supporting Information is available from the Wiley Online Library or from the author.

Acknowledgements

This work has received funding from the German Ministry of Education and Research (BMBF) under grant agreements 16ES1122 (NobleNEMS), and 13N15100 (ACDC) and from the European Union's Horizon 2020 research and innovation programme under grant agreements 829035 (QUEFORMAL), 825272 (ULISSES), and 881603 (Graphene Flagship Core 3). The authors want to than Dr. Cian Bartlam for proofreading the manuscript.

Open access funding enabled and organized by Projekt DEAL.

Conflict of Interest

The authors declare no conflict of interest.

Author Contributions

M.P., G.S.D., and M.C.L. conceived and defined the study. G.S.D. supervised the project. M.P. fabricated $PtSe_2$ layers and conducted Raman measurements. A.S. brought the idea of fabrication of topological substrates and prepared those substrates. O.H. prepared and optimized the rendered graphics. O.H. and T.S.L. measured and analyzed the XPS spectra. M.P. prepared samples for X-SEM, F.G. prepared lamellas for all X-TEM measurements, measured those lamellas, and analyzed the resulting data. K.L. conducted electrical and gas sensing measurements, and analyzed the resulting data. S.P. and J. Bolten prepared SOI waveguide substrates for selective deposition. J. Biba contributed significantly to optimize the process flow of area selective deposition. M.P. performed selective deposition of Al_2O_3 pads and conducted XPS measurements and Raman measurements. S.P., S.S., and A.L.G. applied electrical contacts and conducted optical and electrical measurements, M.C.L, S.S, A.L.G., and S.P. analyzed the resulting data. All authors extensively review and discussed the result. M.P. and G.S.D. wrote the manuscript with input from all authors.

Data Availability Statement

The data that support the findings of this study are available from the corresponding author upon reasonable request.

© 2021 The Authors. Advanced Functional Materials published by Wiley-VCH GmbH

16163028, 2021, 46, Downloaded from https://onlinelibrary.wiley.com/doi/10.1002/adfm.202103936 by CochraneItalia, Wiley Online Library on [29/12/2022]. See the Terms and Conditions (https://onlinelibrary.wiley.com/terms-and-conditions) on Wiley Online Library for rules of use; OA articles are governed by the applicable Creative Commons License

Keywords

2D materials, area selective deposition, chemical sensors, conformal deposition, hybrid devices, infrared photodetectors, platinum diselenide

Received: May 10, 2021
Revised: July 6, 2021
Published online: August 16, 2021

[1] K. S. Novoselov, A. K. Geim, S. V. Morozov, D. Jiang, Y. Zhang, S. V. Dubonos, I. V. Grigorieva, A. A. Firsov, *Science* **2004**, *306*, 666.
[2] L. Li, Y. Yu, G. J. Ye, Q. Ge, X. Ou, H. Wu, D. Feng, X. H. Chen, Y. Zhang, *Nat. Nanotechnol.* **2014**, *9*, 372.
[3] E. Chen, W. Xu, J. Chen, J. H. Warner, *Mater. Today Adv.* **2020**, *7*, 100076.
[4] G. R. Bhimanapati, Z. Lin, V. Meunier, Y. Jung, J. Cha, S. Das, D.i Xiao, Y. Son, M. S. Strano, V. R. Cooper, L. Liang, S. G. Louie, E. Ringe, W. Zhou, S. S. Kim, R. R. Naik, B. G. Sumpter, H. Terrones, F. Xia, Y. Wang, J. Zhu, D. Akinwande, N. Alem, J. A. Schuller, R. E. Schaak, M. Terrones, J. A. Robinson, *ACS Nano* **2015**, *9*, 11509.
[5] J. S. Ponraj, Z.-Q. Xu, S. C. Dhanabalan, H. Mu, Y. Wang, J. Yuan, P. Li, S. Thakur, M. Ashrafi, K. Mccoubrey, Y. Zhang, S. Li, H. Zhang, Q. Bao, *Nanotechnology* **2016**, *27*, 462001.
[6] J. Cheng, C. Wang, X. Zou, L. Liao, *Adv. Opt. Mater.* **2019**, *7*, 1800441.
[7] C. Lan, Z. Shi, R. Cao, C. Li, H. Zhang, *Nanoscale* **2020**, *12*, 11784.
[8] M. C. Lemme, S. Wagner, K. Lee, X. Fan, G. J. Verbiest, S. Wittmann, S. Lukas, R. J. Dolleman, F. Niklaus, H. S. J. van der Zant, G. S. Duesberg, P. G. Steeneken, *Research* **2020**, *2020*, 8748602.
[9] G. Iannaccone, F. Bonaccorso, L. Colombo, G. Fiori, *Nat. Nanotechnol.* **2018**, *13*, 183.
[10] Z. Sun, H. Chang, *ACS Nano* **2014**, *8*, 4133.
[11] M. Long, P. Wang, H. Fang, W. Hu, *Adv. Funct. Mater.* **2019**, *29*, 1803807.
[12] S. Wagner, C. Yim, N. McEvoy, S. Kataria, V. Yokaribas, A. Kuc, S. Pindl, C.-P. Fritzen, T. Heine, G. S. Duesberg, M. C. Lemme, *Nano Lett.* **2018**, *18*, 3738.
[13] C. S. Boland, C. Ó. Coileáin, S. Wagner, J. B. McManus, C. P. Cullen, M. C. Lemme, G. S. Duesberg, N. McEvoy, *2D Mater.* **2019**, *6*, 045029.
[14] S. Yang, C. Jiang, S.-h. Wei, *Appl. Phys. Rev.* **2017**, *4*, 021304.
[15] M. Donarelli, L. Ottaviano, *Sensors* **2018**, *18*, 3638.
[16] A. K. Geim, I. V. Grigorieva, *Nature* **2013**, *499*, 419.
[17] D. Neumaier, S. Pindl, M. C. Lemme, *Nat. Mater.* **2019**, *18*, 525.
[18] R. Clark, K. Tapily, K.-H. Yu, T. Hakamata, S. Consiglio, D. O'Meara, C. Wajda, J. Smith, G. Leusink, *APL Mater.* **2018**, *6*, 058203.
[19] A. J. M. Mackus, M. J. M. Merkx, W. M. M. Kessels, *Chem. Mater.* **2019**, *31*, 2.
[20] D. Akinwande, C. Huyghebaert, C.-H. Wang, M. I. Serna, S. Goossens, L.-J. Li, H.-S. P. Wong, F. H. L. Koppens, *Nature* **2019**, *573*, 507.
[21] B. M. Bersch, S. M. Eichfeld, Y.-C. Lin, K. Zhang, G. R. Bhimanapati, A. F. Piasecki, M. Labella, J. A. Robinson, *2D Mater.* **2017**, *4*, 025083.
[22] S. Balasubramanyam, M. J. M. Merkx, M. A. Verheijen, W. M. M. Kessels, A. J. M. Mackus, A. A. Bol, *ACS Mater. Lett.* **2020**, *2*, 511.
[23] A. J. M. Mackus, A. A. Bol, W. M. M. Kessels, *Nanoscale* **2014**, *6*, 10941.
[24] Z. Lin, A. McCreary, N. Briggs, S. Subramanian, K. Zhang, Y. Sun, X. Li, N. J. Borys, H. Yuan, S. K. Fullerton-Shirey, A. Chernikov, H. Zhao, S. McDonnell, A. M. Lindenberg, K. Xiao, B. J. LeRoy, M. Drndić, J. C. M. Hwang, J. Park, M. Chhowalla, R. E. Schaak, A. Javey, M. C. Hersam, J. Robinson, M. Terrones, *2D Mater.* **2016**, *3*, 042001.
[25] C. Yim, K. Lee, N. McEvoy, M. O'Brien, S. Riazimehr, N. C. Berner, C. P. Cullen, J. Kotakoski, J. C. Meyer, M. C. Lemme, G. S. Duesberg, *ACS Nano* **2016**, *10*, 9550.
[26] Y. Wang, L. Li, W. Yao, S. Song, J. T. Sun, J. Pan, X. Ren, C. Li, E. Okunishi, Y.-Q. Wang, E. Wang, Y. Shao, Y. Y. Zhang, H.-t. Yang, E. F. Schwier, H. Iwasawa, K. Shimada, M. Taniguchi, Z. Cheng, S. Zhou, S. Du, S. J. Pennycook, S. T. Pantelides, H.-J. Gao, *Nano Lett.* **2015**, *15*, 4013.
[27] Y. H. D. Lee, M. Lipson, *IEEE J. Sel. Top. Quantum Electron.* **2013**, *19*, 8200207.
[28] S. Sedky, A. Witvrouw, H. Bender, K. Baert, *IEEE Trans. Electron Devices* **2001**, *48*, 377.
[29] G. Wang, Z. Wang, N. McEvoy, P. Fan, W. J. Blau, *Adv. Mater.* **2021**, *33*, 2004070.
[30] A. Ciarrocchi, A. Avsar, D. Ovchinnikov, A. Kis, *Nat. Commun.* **2018**, *9*, 919.
[31] W. Zhang, J. Qin, Z. Huang, W. Zhang, *J. Appl. Phys.* **2017**, *122*, 205701.
[32] L. Ansari, S. Monaghan, N. McEvoy, C. Ó. Coileáin, C. P. Cullen, J. Lin, R. Siris, T. Stimpel-Lindner, K. F. Burke, G. Mirabelli, R. Duffy, E. Caruso, R. E. Nagle, G. S. Duesberg, P. K. Hurley, F. Gity, *npj 2D Mater. Appl.* **2019**, *3*, 33.
[33] C. Yim, N. McEvoy, S. Riazimehr, D. S. Schneider, F. Gity, S. Monaghan, P. K. Hurley, M. C. Lemme, G. S. Duesberg, *Nano Lett.* **2018**, *18*, 1794.
[34] L. Zeng, S. Lin, Z. Lou, H. Yuan, H. Long, Y. Li, W. Lu, S. P. Lau, D.i Wu, Y. H. Tsang, *NPG Asia Mater* **2018**, *10*, 352.
[35] Y. Zhao, J. Qiao, Z. Yu, P. Yu, K. Xu, S. P. Lau, W. Zhou, Z. Liu, X. Wang, W. Ji, Y. Chai, *Adv. Mater.* **2017**, *29*, 1604230.
[36] L.-H. Zeng, S.-H. Lin, Z.-J. Li, Z.-X. Zhang, T.-F. Zhang, C. Xie, C.-H. Mak, Y. Chai, S. P. Lau, L.-B. Luo, Y. H. Tsang, *Adv. Funct. Mater.* **2018**, *28*, 1705970.
[37] S. M. George, *Chem. Rev.* **2010**, *110*, 111.
[38] R. Gatensby, T. Hallam, K. Lee, N. McEvoy, G. S. Duesberg, *Solid-State Electron.* **2016**, *125*, 39.
[39] K. Lee, R. Gatensby, N. McEvoy, T. Hallam, G. S. Duesberg, *Adv. Mater.* **2013**, *25*, 6699.
[40] A. J. M. Mackus, M. A. Verheijen, N. Leick, A. A. Bol, W. M. M. Kessels, *Chem. Mater.* **2013**, *25*, 1905.
[41] F. Grillo, H. van Bui, J. A. Moulijn, M. T. Kreutzer, J. R. van Ommen, *J. Phys. Chem. Lett.* **2017**, *8*, 975.
[42] M. O'Brien, N. McEvoy, C. Motta, J.-Y. Zheng, N. C. Berner, J. Kotakoski, K. Elibol, T. J. Pennycook, J. C. Meyer, C. Yim, M. Abid, T. Hallam, J. F. Donegan, S. Sanvito, G. S. Duesberg, *2D Mater.* **2016**, *3*, 021004.
[43] J. B. Mc Manus, D. V. Horvath, M. P. Browne, C. P. Cullen, G. Cunningham, T. Hallam, K. Zhussupbekov, D. Mullarkey, C. Ó. Coileáin, I. V. Shvets, M. Pumera, G. S. Duesberg, N. McEvoy, *Nanotechnology* **2020**, *31*, 375601.
[44] B. M. Szydłowska, O. Hartwig, B. Tywoniuk, T. Hartman, T. Stimpel-Lindner, Z. Sofer, N. McEvoy, G. S. Duesberg, C. Backes, *2D Mater.* **2020**, *7*, 045027.
[45] Y. Jung, J. Shen, Y. Liu, J. M. Woods, Y. Sun, J. J. Cha, *Nano Lett.* **2014**, *14*, 6842.
[46] S. S. Han, J. H. Kim, C. Noh, J. H. Kim, E. Ji, J. Kwon, S. M. Yu, T.-J. Ko, E. Okogbue, K. H. Oh, H.-S. Chung, Y. Jung, G.-H. Lee, Y. Jung, *ACS Appl. Mater. Interfaces* **2019**, *11*, 13598.
[47] F. Yavari, N. Koratkar, *J. Phys. Chem. Lett.* **2012**, *3*, 1746.
[48] S.-Y. Cho, Y. Lee, H.-J. Koh, H. Jung, J.-S. Kim, H.-W. Yoo, J. Kim, H.-T. Jung, *Adv. Mater.* **2016**, *28*, 7020.
[49] E. Lee, Y. S. Yoon, D.-J. Kim, *ACS Sens.* **2018**, *3*, 2045.
[50] M. Sajjad, E. Montes, N. Singh, U. Schwingenschlögl, *Adv. Mater. Interfaces* **2017**, *4*, 1600911.
[51] M. O'Brien, K. Lee, R. Morrish, N. C. Berner, N. McEvoy, C. A. Wolden, G. S. Duesberg, *Chem. Phys. Lett.* **2014**, *615*, 6.

© 2021 The Authors. Advanced Functional Materials published by Wiley-VCH GmbH

16163028, 2021, 46, Downloaded from https://onlinelibrary.wiley.com/doi/10.1002/adfm.202103936 by CochraneItalia, Wiley Online Library on [29/12/2022]. See the Terms and Conditions (https://onlinelibrary.wiley.com/terms-and-conditions) on Wiley Online Library for rules of use; OA articles are governed by the applicable Creative Commons License

[52] R. Gatensby, N. McEvoy, K. Lee, T. Hallam, N. C. Berner, E. Rezvani, S. Winters, M. O'Brien, G. S. Duesberg, *Appl. Surf. Sci.* **2014**, *297*, 139.
[53] G. Chen, T. M. Paronyan, A. R. Harutyunyan, *Appl. Phys. Lett.* **2012**, *101*, 053119.
[54] J. Lin, J. Zhong, J. R. Kyle, M. Penchev, M. Ozkan, C. S. Ozkan, *Nanotechnology* **2011**, *22*, 355701.
[55] M. Gautam, A. H. Jayatissa, *Mater. Sci. Eng., C* **2011**, *31*, 1405.
[56] L. A. Currie, *Anal. Chim. Acta* **1999**, *391*, 105.
[57] A. Moudgil, S. Sharma, S. Das, in *2020 IEEE 20th Int. Conf. on Nanotechnology (IEEE-NANO)*, IEEE, **2020**, p. 338, https://ieeexplore.ieee.org/document/9183686/authors#authors.
[58] O. Leenaerts, B. Partoens, F. M. Peeters, *Phys. Rev. B* **2008**, *77*, 125416.
[59] D. J. Late, Y.-K. Huang, B. Liu, J. Acharya, S. N. Shirodkar, J. Luo, A. Yan, D. Charles, U. V. Waghmare, V. P. Dravid, C. N. R. Rao, *ACS Nano* **2013**, *7*, 4879.
[60] S. Zhao, J. Xue, W. Kang, *Chem. Phys. Lett.* **2014**, *595*, 35.
[61] T. Zhang, S. Mubeen, N. V. Myung, M. A. Deshusses, *Nanotechnology* **2008**, *19*, 332001.
[62] G. F. Cerofolini, L. Meda, *Appl. Surf. Sci.* **1995**, *89*, 351.
[63] W. L. Gladfelter, *Chem. Mater.* **1993**, *5*, 1372.
[64] D. Schall, C. Porschatis, M. Otto, D. Neumaier, *J. Phys. D: Appl. Phys.* **2017**, *50*, 124004.
[65] X. Wang, Z. Cheng, K. Xu, H. K. Tsang, J.-B. Xu, *Nat. Photonics* **2013**, *7*, 888.

© 2021 The Authors. Advanced Functional Materials published by Wiley-VCH GmbH

16163028, 2021, 46, Downloaded from https://onlinelibrary.wiley.com/doi/10.1002/adfm.202103936 by CochraneItalia, Wiley Online Library on [29/12/2022]. See the Terms and Conditions (https://onlinelibrary.wiley.com/terms-and-conditions) on Wiley Online Library for rules of use; OA articles are governed by the applicable Creative Commons License